Int J Appl Earth Obs Geoinformation 93 (2020) 102197

Contents lists available at ScienceDirect

Int J Appl Earth Obs Geoinformation

journal homepage: www.elsevier.com/locate/jag

Prediction of topsoil properties at field-scale by using C-band SAR data

Marisa B. Domenech[a,*], Nilda M. Amiotti[a,b], José L. Costa[c], Mauricio Castro-Franco[d]

[a] Departamento de Agronomía, Universidad Nacional del Sur (UNS), San Andrés 800, Bahía Blanca, 8000, Buenos Aires, Argentina
[b] CERZOS, Universidad Nacional del Sur (UNS)-CONICET, Bahía Blanca, Argentina
[c] Instituto Nacional de Tecnología Agropecuaria INTA, EEA Balcarce, Ruta 226, Km 73.5, Balcarce, Argentina
[d] Agronomy Program, Colombian Sugarcane Research Center (Cenicaña), Experimental Station via Cali-Florida, Km 26, Colombia

ARTICLE INFO

Keywords:
Digital soil mapping
Sentinel 1
Random Forest
Precision agriculture
Soil apparent electrical conductivity
Radar Remote Sensing
Conditioned Latin hypercube sampling

ABSTRACT

Designing and validating digital soil mapping (DSM) techniques can facilitate precision agriculture implementation. This study generates and validates a technique for the spatial prediction of soil properties based on C-band radar data. To this end, (i) we focused on working at farm-field scale and conditions, a fact scarcely reported; (ii) we validated the usefulness of Random Forest regression (RF) to predict soil properties based on C-band radar data; (iii) we validated the prediction accuracy of C-band radar data according to the coverage condition (for example: crop or fallow); and (iv) we aimed to find spatial relationship between soil apparent electrical conductivity and C-band radar. The experiment was conducted on two agricultural fields in the southern Argentine Pampas. Fifty one *Sentinel 1* Level-1 GRD (Grid) products of C-band frequency (5.36 GHz) were processed. VH and VV polarizations and the dual polarization SAR vegetation index (DPSVI) were estimated. Soil information was obtained through regular-grid sample scheme and apparent soil electrical conductivity (ECa) measurements. Soil properties predicted were: texture, effective soil depth, ECa at 0-0.3m depth and ECa at 0-0.9m depth. The effect of water, vegetation and soil on the depolarization from SAR backscattering was analyzed. Complementary, spatial predictions of all soil properties from ordinary cokriging and Conditioned Latin hypercube sampling (cLHS) were evaluated using six different soil sample sizes: 20, 40, 60, 80, 100 and the total of the grid sampling scheme. The results demonstrate that the prediction accuracy of C-band SAR data for most of the soil properties evaluated varies considerably and is closely dependent on the coverage type and weather dynamics. The polarizations with high prediction accuracy of all soil properties showed low values of σ_{VV}^{o} and σ_{VH}^{o}, while those with low prediction accuracy showed high values of σ_{VV}^{o} and low values of σ_{VH}^{o}. The spatial patterns among maps of all soil properties using all samples and all sample sizes were similar. In conditions when summer crops demand large amount of water and there is soil water deficit backscattering showed higher prediction accuracy for most soil properties. During the fallow season, the prediction accuracy decreased and the spatial prediction accuracy was closely dependent on the number of validation samples. The findings of this study corroborates that DSM techniques at field scale can be achieved by using C-band SAR data. Extrapolation y applicability of this study to other areas remain to be tested.

1. Introduction

There is an increasing demand for producing crops highly efficient in the use of agricultural supplies and water resources (Van Ittersum et al., 2013). To achieve this, spatio-temporal dynamics of soil properties and their interaction with climate and crop management variables have became essential information. Actually, soil property maps are generally scarce because conventional methods in most agricultural zones of the world, which are difficult, costly and destructive (Hartemink et al., 2008). So, novel, rapid, efficient, accurate and economic methods to create soil property maps at field scale should be generated and validated.

Numerous studies have reported that remote sensing data can help to generate fast, accurate and low-cost soil maps at multi-scale, by providing precise, representative and timely information on soil-forming factors (Boettinger, 2010; Lagacherie et al., 2006). Several soil properties show high spectral reflectance in the VIS, NIR and SWIR (0.4–2.5 μm) spectral regions. Thus, information from that spectral response has been widely used to generate and validate soil properties maps (Boettinger et al., 2008; Hartemink et al., 2008). Other spectral regions so far little used to generate soil properties maps, such as radar remote sensing and particularly a portion of low frequency in the

* Corresponding author.
E-mail address: marisabdomenech@gmail.com (M.B. Domenech).

https://doi.org/10.1016/j.jag.2020.102197
Received 17 October 2019; Received in revised form 5 June 2020; Accepted 10 July 2020

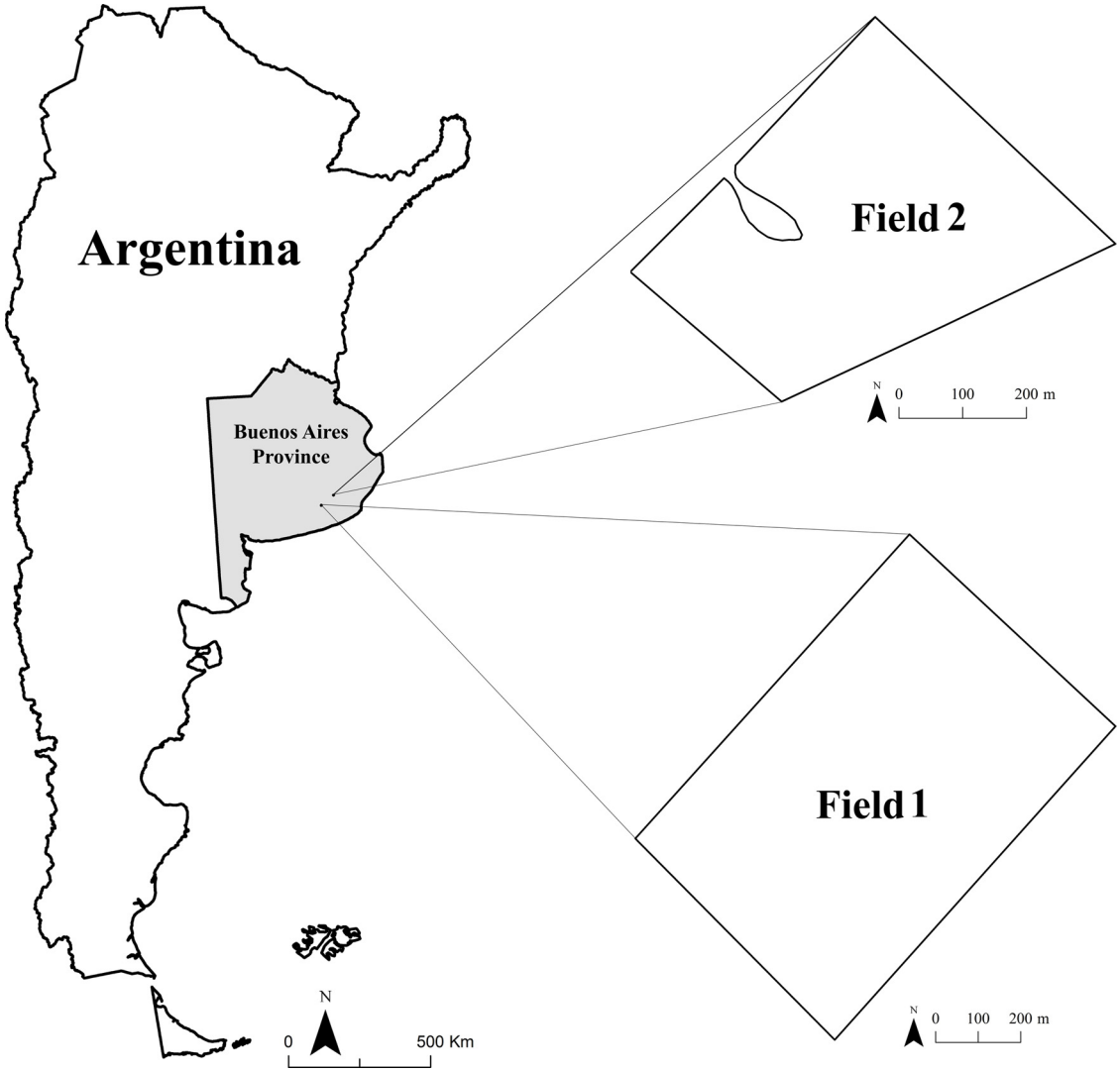

Fig. 1. Location of experimental farm fields.

microwave spectrum (P to L-band). This is partly due to the complexity, diversity and difficulty of Synthetic Aperture Radar (SAR) data interpretation (Veloso et al., 2017), and also they are available in multiples frequencies and incidence angles. Data interpretation includes taking into account spatio-temporal dynamics of soil and crop properties and particularly their sensitivity to soil moisture changes, surface roughness and vegetal biomass. An efficient monitoring of spatio-temporal relationship of soil and crop properties allows a better understanding in the soil properties role on yield generation and agricultural supplies use (Birrell et al., 1996; Dang et al., 2011; Lobell et al., 2015). To achieve this, high spatial and temporal resolutions satellite imagery time series are required (McNairn and Shang, 2016). At present, the European Space Agency (ESA) granted the access to large SAR datasets obtained from Sentinel 1 satellite constellation, including Sentinel 1-A and Sentinel 1-B. The aim of Sentinel-1 is to provide multi-temporal series of SAR imagery (C-Band) with temporal resolution of 10 days. Sentinel 1-A was launched in April 2016, while Sentinel 1-B was launched in June 2015 (Berger et al., 2012). Simultaneously, ESA through Sentinel 2-B constellation launched in June 2015 provides optical images free of charge with temporal resolution of 5 days. The dense time series of SAR and optical data offer a unique opportunity to systematically characterize multiple soil and crop properties, at diverse spatial scales.

An effective strategy to estimate and generate soil properties maps is to analyze the systematic relationship between spatio-temporal dynamics of soil moisture and multiple soil properties. Zribi et al. (2011) developed an empirical model ($R^2 \sim 0.6$) to predict clay content at regional scale in semiarid conditions using spatio-temporal dynamics of SAR data (X-Band) with shallow incidence angles (35°) and horizontal polarization. On the other hand, Gorrab et al. (2015) proposed a methodology combing multi-temporal X-band SAR data (TerraSAR-X) for the retrieval of Surface soil moisture and texture at a high spatial scale. These authors reported two empirical models ($R^2 > 0.62$) to predict soil moisture values and the soil texture components over 36 tests fields. In general, the soil moisture and ground-surface conditions in farm fields have high spatio-temporal dynamics. The intensity of such dynamics usually depends on soil properties such as roughness, texture, structure, organic matter content, porosity, apparent density, runoff, infiltration and salinity. These systematic relationships could determine the behavior of SAR backscatter coefficients and thus, be feasible to optimize the spatial prediction of multiple soil properties. For example, the intensity of backscattered radar signals decreased in lower proportion in sandy than clay soils because the former have higher evaporation and infiltration rates (Zribi et al., 2011). Thus, analyzing and determining the relationship between spatio-temporal spectral information from radar remote sensing, soil moisture and soil properties would improve the development of efficient to generate soil properties maps (Han et al., 2017).

The aim of this study was to generate and validate a technique for

the spatial prediction of soil properties based on C-band radar data. To this end, (*i*) we focused on working at farm-field scale, analyzing the behavior of SAR backscatter and NDVI for wheat, soybean, maize and sunflower with similar management practices and climate conditions; (*ii*) we validated the usefulness of Random Forest regression to predict soil properties based on C-band radar data; (*iii*) we validated the prediction accuracy of C-band radar data according to the coverage condition (for example: crop or fallow); and (*iv*) we aimed to find spatial relationship between soil apparent electrical conductivity and C-band radar.

2. Materials and methods

2.1. Study area and experimental farm fields

The Argentine Pampas have more that 50 Mha a suitable for crop and cattle production, which runs from 30° to 40 °S, 57° to 68 °W. The relief is flat or slightly rolling. The soils present a wide range of variation in depth, texture, and organic matter (Alvarez and Lavado, 1998). The Pampas is divided into five homogeneous ecological subregions according to their rainfall, topography and soil quality patterns: Rolling Pampas, Central Pampas, Southern Pampas, Flooding Pampas and Mesopotamian Pampas (Pérez et al., 2015). Actually, The Pampas is one of the most important areas for crop production in the world because of its extension and yield potential (Alvarez, 2009).

The study was carried in the southeastern Pampas of Argentina (Fig. 1). This zone is the part of the Southern Pampas situated between the Salado River basin to the north, the Colorado River basin to the south, the Radial Depressed Area to the west, and the Atlantic Ocean to the east (Barral and Oscar, 2012). The predominant crop sequences include maize, soybean or sunflower in summer and wheat or barley in winter (Sadras and Calviño, 2001). The topography, soil quality, problems of salinity, water drainage and flood risk of the southeastern Pampas have small differences. The soils are classified as Typic Argiudolls and Petrocalcic Argiudolls (USDA Taxonomy) with less than 2 % slope, with udic soil moisture regime (INTA, 2010). These soils generally, have a loam texture in the surface layer (0 – 0.25 m depth), loam to clay loam in subsurface layers (0.25–1.1 m depth) and sandy loam below 1.1 m depth. The effective soil depth ranges from 0.4–1.2 m to 0.1–1.1 m. The climate is classified as mesothermal subhumid-humid (Thornthwaite classification). The mean annual temperature is ~14 °C (Pascale and Damario, 2004). The precipitation pattern is isohygrous and the mean annual precipitation is 913 mm, with maxima (> 60 %) in October and March. The mean potential evapotranspiration is 894 mm.

Fig. 1 shows the localization of the two experimental farm fields used in this study. Field 1 has 64.8 ha and field 2 has 23.4 ha. Both were selected according to their variability in elevation, landscape position, surface reflectance, crop yield and soil types which represent the typical conditions in the southeastern Pampas of Argentina. The clay content at 20 cm depth ranges from 28 to 38 % for field 1 and from 18 to 27 % for field 2. Both fields had similar tillage system (no-till), fertilization management and crop rotation. Also, they have not irrigation system. Crop rotation was summer crop (maize, sunflower or soybean) - winter crop (wheat or barley) - fallow - summer crop. In most crops, nearly all aboveground biomass was exported as grain.

The field 1 is located en Loberia District. Agricultural seasons considered in this study were: winter crop 2016 (September to December 2016) cultivated with wheat, fallow 2017 with stubble aboveground (June to September 2017) and summer crop 2017 – 2018 cultivated with sunflower (November 2017 to March 2018). Field 2 is located in Balcarce District. Agricultural seasons considered in this study were: summer crop 2016 – 2017 (November 2016 to March 2017) and 2017 – 2018 (November 2017 to March 2018), cultivated with soybean and fallow 2017 (June–September 2017).

2.2. Precipitation data and water balance

Precipitation data were obtained from weather stations close to the farm field site. The hydric balance was determined according to Della Maggiora et al. (2002). Actual and maximum evapotranspiration were calculated using the crop coefficients reported by Allen et al. (1998). Water holding (mm cm^{-1}) and soil water availability (mm cm^{-1}) were calculated using the model proposed by (Travasso and Suero, 1994). Maximum soil water storage was estimated by the product between soil depth and the total soil water storage capacity (Travasso and Suero, 1994). Actual soil water content was calculated using the balance between precipitation and evapotranspiration. When the soil water content is a 50 % smaller than water availability, the actual evotranspiration is less than the maximum evapotranspiration. Thus, water deficiency was estimated as the difference between the maximum and actual evapotranspiration.

2.3. Remote sensing data

2.3.1. C-band SAR data

C-band SAR (5.36 GHz) *Sentinel 1* is a product of the European Space Agency (ESA). In this study, a total of 51 *Sentinel 1* radar images (27 for field 1 and 24 for field 2) were downloaded from the Copernicus Open Access Hub (ESA - https://copernicus.eu/dhus/#/home), in the Interferometric Wide swath mode. *Sentinel 1* was designed with one transmitter and two receiver chains. Thus, it supports operation in both single (HH or HV) and dual polarizations (HH and HV or VV and VH). In this case, we used the Level-1 GRD (Grid) product and VH and VV polarizations, which have been reported for the study of land application (Periasamy, 2018). SAR data were acquired with 250 km total swath in a spatial dimension. All images were acquired in descending mode. The incidence angle varied from 39.6° to 39.7°. The relative orbit number (RON) was 23 and 170 for Sentinel 1A and 1B, respectively. Acquisition time varied from 9:06 to 9:07 am.

Sentinel 1 images were processed using the open-code software *Sentinel 1*- Toolbox SNAP (http://step.esa.int/main/download) in five steps. The first step was to select the area of interest using the *subset* function. Then, a radiometric calibration was performed, in which values of digital numbers were transformed into backscattering in power format (σ^{o}_{VV} and σ^{o}_{VH}). Third, a multilooking procedure was applied with a number of looks equal to 1. Fourth, the speckle reduction was performed using a 7 × 7 enhanced Lee filter. Finally, a geometric calibration was applied using Range Doppler Correction, based on the information obtained from the orbit state vector in the metadata, radar timing annotations, slant-to ground range conversion parameters and reference digital elevation model (DEM) data. In this study, the NASA´s Shuttle Radar Topography Mission (SRTM) DEM at 3 arc-seconds was used. The final product was reprojected into the UTM 20 South coordinate system.

2.3.2. Optical data

A total of thirty-eight satellite images from Sentinel-2 were used in this study. The main selection criteria was the lack of cloudiness. Optical images have been downloaded from the cloud-based geospatial processing platform Google Earth Engine (GEE) (Gorelick et al., 2017). Sentinel-2 data is provided in GEE as a Level-1C product representing Top-of-Atmosphere reflectance (TOA). For field 1, eighteen images were processed between Sep-Dec/2016 (Winter Crop 2016 period), Jun-Sep/2017 (Fallow 2017 period) and Nov/2017 – Feb/2018 (Summer Crop 2017–2018 period). For field 2, twenty optical images were used between Nov/2016 – Feb/2017 (Summer Crop 2016 – 2017 period), Jun-Sep/2017 (Fallow 2017 period) and Nov/2017 – Feb/2018 (Summer Crop 2017 – 2018 period) (See Fig. 3). Images have been acquired with a spatial resolution of 10 m in three spectral bands (green, red and near infrared).

The Normalized Difference Vegetation Index (NDVI) was computed

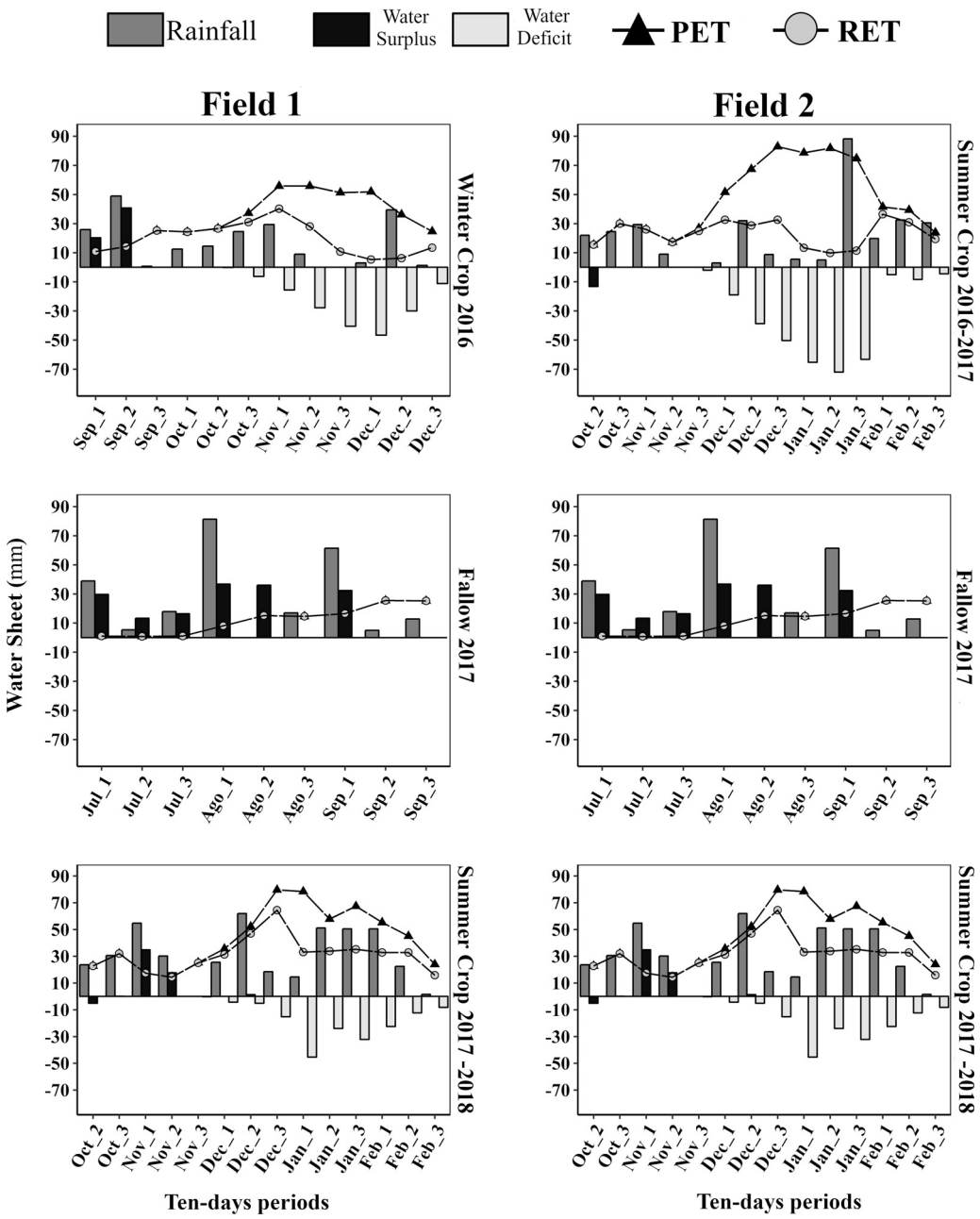

Fig. 2. Hydric balance dynamics between experimental fields and crop season.

within GEE. NDVI represents the difference between the reflectance of NIR band and the red band from the visible spectrum, being previously used in numerous land cover applications, due to be sensitive to identify phenologycal differences in crops (d'Andrimont et al., 2020; Kriegler et al., 1969). In this study, NDVI was used to capture the phenological development of crops within fields.

2.4. Soil sampling scheme and measurement of the apparent soil electrical conductivity

The soil was sampled by means of a 50 × 100 m regular grid for field 1 and a 50 × 50 m grid for field 2. A total of 126 and 79 soil samples were collected from each field. These sizes of grids are commonly used by surveyors and farmers in intensive sampling for soil fertility assessment at farm scale (Castro Franco et al., 2015). The effective soil depths were determined at the nodes of the grids, by using a truck-mounted Giddings Soil Sampler (Model XHDGSRPST Giddings Machine Co., Fort Collins, CO, USA). The pitcher barrel sample was about 1.5 m in length. Soil sample depths were measured and marked on the pitcher barrel to determine effective soil depth. The soil was sampled by genetic soil horizon from 0 to 20 cm. All soil analyses were conducted in the laboratory of the National Institute of Agricultural Technology (INTA), Experimental Station Balcarce, Argentina. The soil texture was analyzed by the Robinson method (Gee and Bauder, 1986; Robinson, 1922). Complementarily, apparent soil electrical conductivity (ECa) was measured using a Veris® 3100 sensor (Veris Technologies Inc., Salina, KS, USA). This sensor is configured as a Wenner array, an arrangement commonly used for geophysical resistivity surveys. The system records ECa in mS m^{-1} by electrical resistivity at shallow depth (0 − 0.3 m, ECa 0 − 0.3 m) and deep depth (0 − 0.9 m, ECa 0 − 0.9 m) (Domenech et al., 2017). ECa measurements were made along parallel transects approximately 20 m apart on the surface of the experimental fields. A handheld GPS Trimble® GeoXT™ with submeter accuracy was used to georeference the ECa measurements. Latitude,

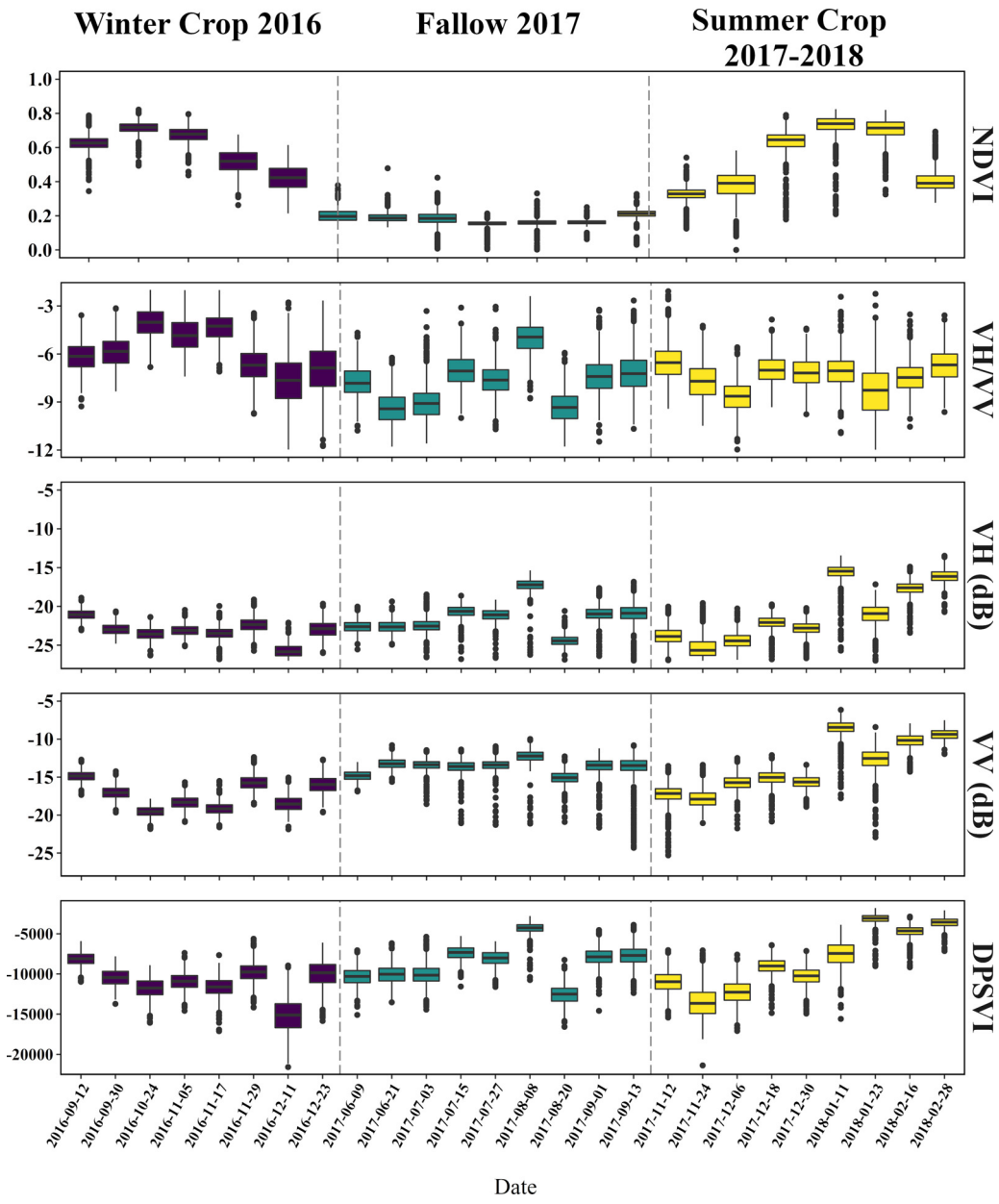

Fig. 3. Temporal dynamics of VV and VH polarizations and DPSVI during crop season for the field 1.

longitude, ECa 0 – 0.3 m and ECa 0 – 0.9 m data were recorded in a CSV text file and transferred to GIS software for analysis. For more details of ECa measurements with the Veris® 3100 sensor, see Corwin and Lesch (2003) and Corwin and Lesch (2005).

Experimental variograms were computed to describe the spatial variation of ECa, following the procedure proposed by Diggle and Ribeiro (2007). The adjusted experimental variogram was used to interpolate ECa by ordinary kriging in each field. The R package "geoR" was used to conduct the geostatistical interpolation (R Core Team, 2016). Finally, a 10 × 10 m grid square size was chosen for output maps.

2.5. Dual polarization SAR vegetation index (DPSVI)

Soil spatial patterns at field scale usually determine the spatial distribution of plant biomass (Boettinger et al., 2008). Thus, the effect of vegetation on the SAR backscattering signal could be a useful auxiliary variable to determine the spatial pattern of soil properties (Boettinger, 2010; Hartemink et al., 2008). This may be used in farm fields where the main surface is covered by the crop biomass.

The DPSVI (Periasamy, 2018; Periasamy et al., 2019) is a physical scattering model which represents the presence of terrestrial vegetation based on the concept of "Degree of Depolarization". In farm field conditions, changes in the biomass may determine variations in the polarization magnitude. In that context, the DPSVI is an alternative not only to the Radar Vegetation Index but also to other vegetation indices (Vreugdenhil et al., 2018), because it represents the terrestrial vegetation obtained from dual polarimetric data (VH and VV) acquired from the *Sentinel 1* constellation.

The DPSVI is a function of an inverse diagonal relationship between σ_{vv} and σ_{vh}, the degree of dual de-polarization and cross-polarized energy (σ_{vh}) (Periasamy, 2018). The function was executed from radiometrically calibrated SAR data whose backscattering values are in linear power units:

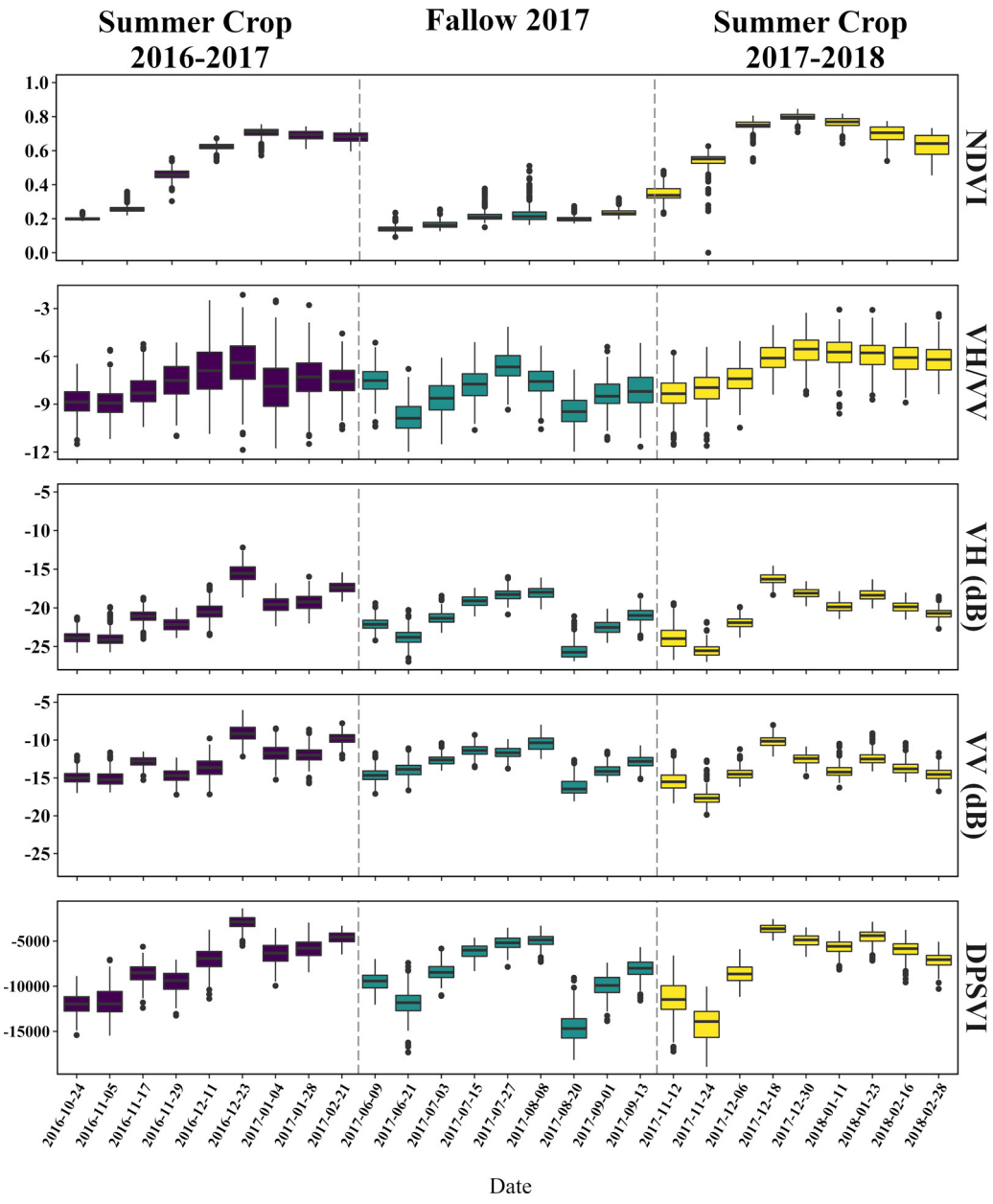

Fig. 4. Temporal dynamics of VV and VH polarizations and DPSVI during crop season for the field 2.

$$DPSVI = \frac{\sigma_{vh(i)}\begin{bmatrix}(\sigma_{vv(max)}\sigma_{vh(i)} - \sigma_{vv(i)}\sigma_{vh(i)} + \sigma^2_{vh(i)})+\\(\sigma_{vv(max)}\sigma_{vv(i)} - \sigma^2_{vv(i)} + \sigma_{vh(i)}\sigma_{vv(i)})\end{bmatrix}}{\sqrt{2} * \sigma_{vv(i)}}$$

where:

$\sigma_{vh(i)}$ and $\sigma_{vv(i)}$ are the backscattering coefficient values of the i^{th} pixel in the cross-polarized and co-polarized (*vh* and *vv*) SAR products, respectively, and $\sigma_{vv(max)}$ is the maximum backscattering coefficient value in the co-polarized (*vv*) SAR product.

2.6. Predictive importance of C-band radar and DPSVI data by date

The Random Forest (RF) algorithm (Breiman, 2001) to determine the predictive importance of the C-band radar and DPSVI data by date to predict soil properties in both experimental farm fields, because several soil mapping studies have demonstrated that this algorithm has great ability to provide predictor importance metrics from auxiliary information (Castro Franco et al., 2015; Genuer et al., 2010; Grömping, 2009; Ließ et al., 2012).

The RF algorithm uses numerous decision trees (n_{trees}) (e.g., CART or C4.5 algorithms) to establish a ranking of predictive importance order. Each tree is constructed using bootstrap sampling, which is approximately 2/3 of the available data. The remaining 1/3 of available data are referred to as out-of-bag (*OOB*) and the proportion of misclassification of these samples (OOB_{error}) can be used as a measure of generalization errors (Breiman, 2001). At each binary split, the variable of C-band radar and DPSVI data by date that produces the best split is chosen from a random subset of the entire variable set. The number of predictors in each random subset is called *mtry*. The optimal n_{trees} and *mtry* must be identified by the user. To determine the predictive importance of each predictor, the RF algorithm generates two quantitative metrics: the *Increased Mean Square Error* (*%IncMSE*) and the *Increased Purity Index* (*IncNodePurity*). *%IncMSE* is a metric that represents the deterioration of the prediction accuracy of the model when each predictor is replaced and this random replacement changes the computed value significantly. Lower *%IncMSE* indicates lesser predictor

Table 1
Percentage of explained variance for each soil properties using Random Forest (RF) regressions executed by field and season.

Field	Soil property	Season		
		Winter Crop 2016	**Fallow 2017**	**Summer Crop 2017_2018**
		Explained Variance (%)		
Field 1	Clay content	47.20	10.45	34.09
	Silt content	62.54	27.78	35.26
	Sand content	62.47	19.98	40.54
	Soil Depth	69.12	18.67	37.34
	ECa_0 − 0.3 m*	57.09	14.83	35.07
	ECa_0 − 0.9 m*	55.11	23.56	35.24
		Summer Crop 2016 − 2017	**Fallow 2017**	**Summer Crop 2017 − 2018**
		Explained Variance (%)		
Field 2	Clay content	57.21	54.95	62.38
	Silt content	54.76	61.87	63.84
	Sand content	57.70	61.83	62.11
	Soil Depth	56.11	50.20	65.67
	ECa_0 − 0.3 m*	53.19	46.56	53.32
	ECa_0 − 0.9 m*	41.49	30.02	36.11

**ECa_0 − 0.3 m*: Soil apparent electrical conductivity at 0 − 0.3 m depth; *ECa_0 − 0.9 m*: Soil apparent electrical conductivity at 0 − 0.9 m depth.

importance. On the other hand, *IncNodePurity* is a metric of the increase in homogeneity of a sample based on splitting the samples from a particular predictor. For more details of the RF algorithm, see Breiman (2001) and Genuer et al. (2010).

The RF algorithm was performed with the R (v3.4.4) package "*randomForest*" (Liaw and Wiener, 2002; R Core Team, 2016) and was run 10 times with C-band radar and DPSVI data by date as predictors, and soil properties as the target variable. The mean of the predictor importance was estimated across these 10 runs. Finally, a dotchart of relative importance was generated from *%IncMSE* of C-band radar and DPSVI data by date and soil property. *%IncMSE* is a metric usually used to select predictors and thus differentiate important from no-important predictors (Genuer et al., 2010).

2.7. Prediction accuracy of soil properties

A soil sampling scheme based on the conditioned Latin Hypercube algorithm (cLHS) (Minasny and McBratney, 2006) was evaluated using a size of 100 samples. cLHS is a random stratified procedure that selects sampling locations across a range of auxiliary variables (Minasny and McBratney, 2006; Roudier et al., 2012). cLHS is constructed by random sampling from the cumulative distribution of auxiliary variable data using a simulated annealing optimization approach, which additionally focuses on preserving the correlation between the auxiliary variables in the sample set selected (Castro Franco et al., 2015). The cLHS algorithm was run using the R package "*clhs*" with the C-band radar or DPSVI data with the highest predictive accuracy as auxiliary variables (R Core Team, 2016).

The accuracy of soil property maps with each soil sampling scheme was assessed by comparing the predicted soil property values with the measured soil property values. The following error metrics were calculated based on the number of soil samples: coefficient of determination (R^2) (Eq. (3)), Root Mean Square Error (RMSE) (Eq. (4)) and Lins´s Concordance Correlation Coefficient (ρ_c) (Eq. (5)). These error metrics were calculated as:

$$R^2 = \frac{\sum_{i=1}^{n}(y_i - \bar{x})}{\sum_{i=1}^{n}(x_i - \bar{x})} \quad (3)$$

$$RMSE = \sqrt{\frac{1}{n}\sum_{i=1}^{n}(y_i - x_i)^2} \quad (4)$$

$$\rho_c = \frac{2S_{xy}}{S_x^2 + S_y^2 + (\bar{x} - \bar{y})^2} \quad (5)$$

where $S_x^2 = \frac{1}{n}\sum_{i=1}^{n}(x_i - \bar{x})^2$, $S_y^2 = \frac{1}{n}\sum_{i=1}^{n}(y_i - \bar{y})^2$, and $S_{xy} = \frac{1}{n}\sum_{i=1}^{n}(x_i - \bar{x})(y_i - \bar{y})$. For all the equations, $\bar{x}$ and $\bar{y}$ are the mean value for samples x (measured soil property) and y (predicted soil property) of the number of samples n, x_i and y_i are paired ith values from the samples x and y.

Generally, a good model will have an RMSE close to 0 and an R^2 close to 1. RMSE measures the average error (or accuracy) of the prediction, whereas R^2 measures the agreement between measured and predicted data. Finally, ρ_c assesses the covariation and correspondence between measured and predicted data. This metric combines measures of both precision and bias to determine how far the measured data deviate from the line of perfect concordance, which is 1:1. The value of this metric is scaled between 1 and - 1, as follows: a value < 0.60 denotes poor agreement, a value between 0.60 and 0.75 denotes moderate agreement, a value between 0.75 and 0.90 substantial agreement and a value > 1 denotes perfect agreement (Castro-Franco et al., 2017; Viscarra Rossel et al., 2015).

3. Results and discussion

3.1. Climate conditions

Hydric balance was used to support the analysis and interpretation of temporal series of SAR backscatter and NDVI. This analysis was carried out separately for all coverage conditions. In that context, Fig. 2 shows the hydric balance estimated for wheat as the winter crop 2016, the fallow 2017 and sunflower as the summer crop 2017 − 2018 for field 1, and that estimated for soybean as the summer crop 2016 − 2017, the fallow 2017 and soybean as the summer crop 2017 − 2018 for field 2. In both fields, crop water deficits occurred at the flowering stage. In field 1, the winter crop 2016 and the summer crop 2017 − 2018 were affected by the water deficits during November 2016 and January 2018, respectively, whereas in field 2, the summer crops 2016 − 2017 and 2017 − 2018 were affected by the water deficit during January, being this more severe in 2016 − 2017. In both fields, there was an excess water condition during the fallow period.

3.2. SAR backscattering and DPSVI temporal series

3.2.1. Field 1

Fig. 3 shows the temporal series of NDVI, SAR backscattering and DPSVI in all coverage conditions (crops and fallow) for field 1. Wheat as the winter crop 2016 period was sown on 15th July, emergence occurred on 24th August and the crop was harvested on 15th December. Sunflower as the summer crop 2017 − 2018 period was sown on 18th September, emergence occurred on 5th October and the crop was harvested on 4th April 2018. VH/VV ratio was more sensitive to changes in biomass during wheat development than for sunflower. In wheat, NDVI starts increasing after the emergence of plants, then achieves the highest value during heading and decreasing at the ripening stage. During the wheat development stage, a similar temporal behavior profile between NDVI and VH/VV ratio was observed. On the contrary, VH and DPSVI did not follow a similar temporal behavior profile during the wheat growth and development.

A temporal correspondence between VH/VV ratio and NDVI during wheat development was expected because similar results have been previously reported (Mattia et al., 2003; McNairn and Shang, 2016; Veloso et al., 2017). During the first weeks of September (~50 days after sowing - tillering), the medians ranged from 0.6 to 0.7 for NDVI, and -7 to -6 for VH/VV ratio, according to reported by Song and Wang, 2019. In this stage, fresh biomass accumulation is high and stable. Then, during early October (~80 days after sowing -booting) and until

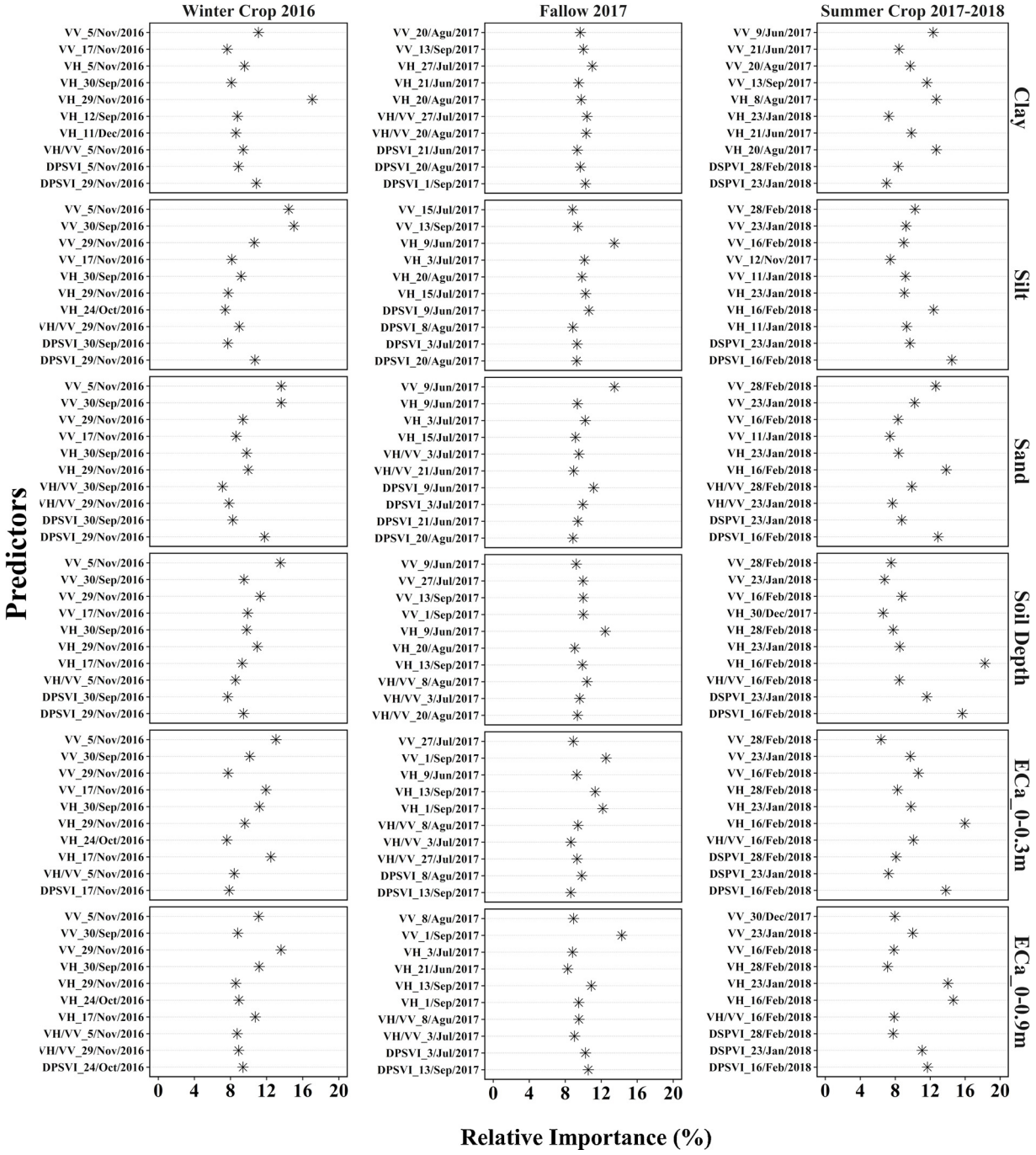

Fig. 5. Relative importance of VV and VH polarizations and DPSVI during crop season for each soil properties predicted for the field 1.

the second week of November (~117 days after sowing - heading) NDVI and VH/VV ratio showed the highest values, > 0.8 and > −4.5, respectively. Also, VV values were the lowest, according to Mattia et al., 2003. This result was expected because VV has a detrimental effect at the tillering stage in wheat, due to an increase in the attenuation caused by the vertical structures of wheat stems (Veloso et al., 2017). In the first week of December (ripening) NDVI and VH/VV ratio showed the lowest values because it was the previous harvest season. In general, NDVI and VH/VV ratio stability was slightly variable during all wheat crop cycle. During the temporal series, the increase and decrease of the curve were related to the wheat development. Veloso et al., 2017 reported that VH/VV ratio is always more correlated to the fresh biomass than to the photosynthesis activity. However, in the present result cannot separate the difference correlation for fresh biomass and the photosynthesis activity.

For sunflower, there was not observed a similar temporal behavior between NDVI and VH/VV ratio. Previously, Veloso et al. (2017) had reported that the VH/VV ratio is not a recommended index for sunflower monitoring. The present results suggest that the unique stem growth of sunflower do not let an increase in the attenuation and thus, VV not decrease. In that situation, the VV behavior limits the prediction accuracy for biomass using the VH/VV ratio. VH, VV and DSPVI increase from the grain filling stage. This can be due to stem structure loss biomass and chlorophyll content decreasing the attenuation caused by stem and thus VV and VH increase. So, it is probably that the increase in VV and VH in this stage could be use as a monitoring index for sunflower physiological maturity, which could be analyzed in further studies.

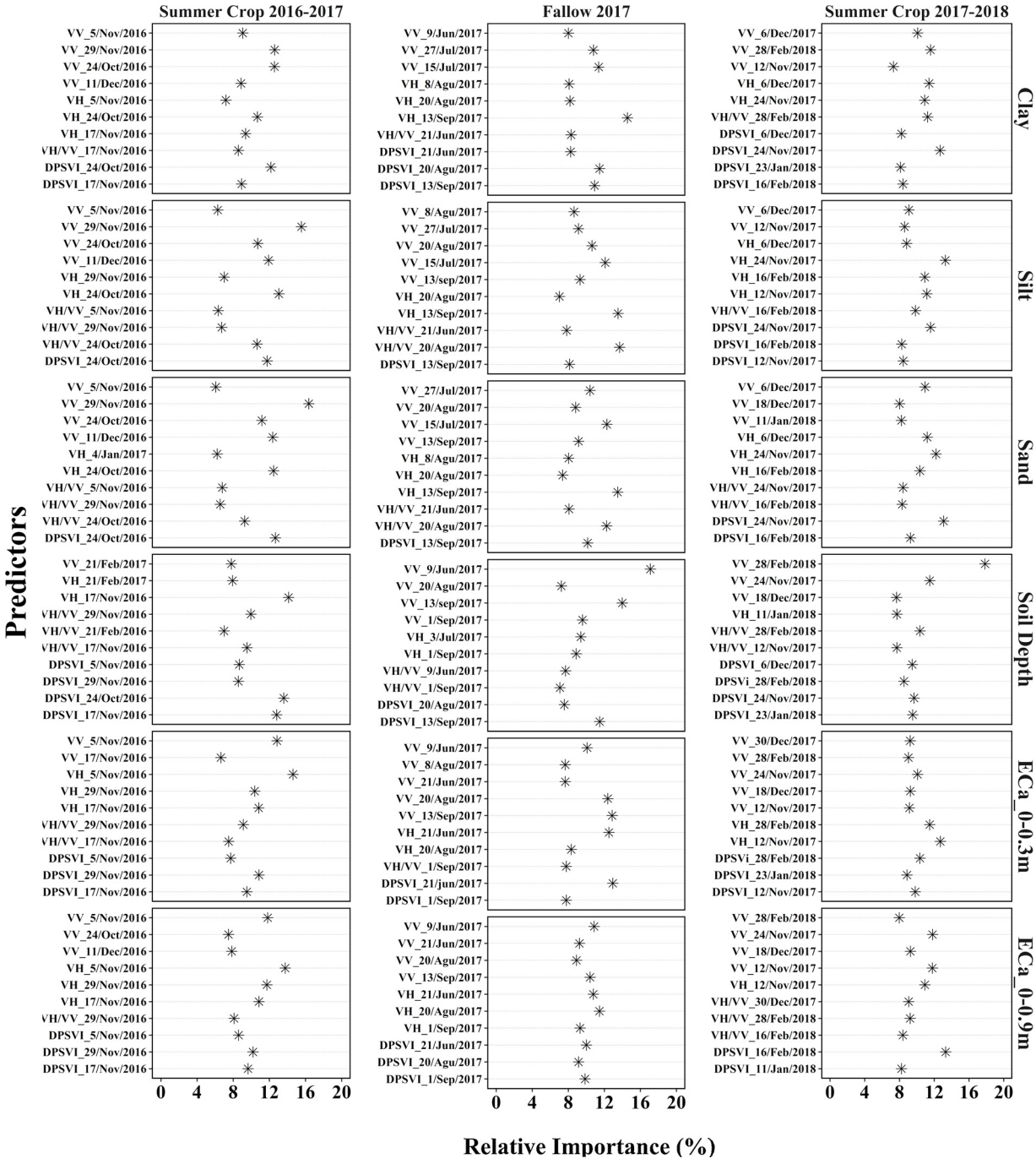

Fig. 6. Relative importance of VV and VH polarizations and DPSVI during crop season for each soil properties predicted for the field 2.

3.2.2. Field 2

In the field 2. NDVI, VH/VV ratio and DPSVI had a similar temporal behavior during soybean development as the summer crop 2016 – 2017 and 2017 – 2018 periods, respectively (Fig. 4). NDVI and VH/VV ratio start increasingly until the first week in January during summer crop 2016 – 2017 period. Then, NDVI was steady while VH/VV ratio decreased. During summer crop 2017 – 2018 period, NDVI and VH/VV ratio increased until the first week in January. Then, both were steady. VH and VV showed similar temporal behavior in both periods, especially during soybean growth and senescence stages which has been previously reported (Veloso et al., 2017). Likewise, DPSVI also had a similar behavior between summer crop periods which has not been previously reported for soybean crop. After flowering, DPSVI showed a decrease in the summer crop 2017 – 2018 period, while cannot be detected in the summer crop 2016 – 2017 period. Differences of VH/VV ratio and DPSVI between summer crop periods at this stage are explained by changes in soil moisture which reduce the effect of interaction soil-vegetation on the SAR backscattering (Zribi et al., 2011). Note that during the summer crop 2016 – 2017 period, soil water available after flowering was less than in the summer crop 2017 – 2018 period (see Fig. 2). For the fallow 2017 period, temporal variation in VH, VV, VH/VV and DPSVI were slight which can be also due to rainfall events and soil water content dynamics. Except for the VH/VV ratio in the summer crop 2016 – 2017 period, variances of all indices within dates were similar. This is because soybean has low height and number of stems per surface unit, so that produce a similar attenuation effect of the soil and vegetation on the backscattered signal (Veloso et al., 2017).

The results reported for the field 2 confirm: (*i*) that SAR

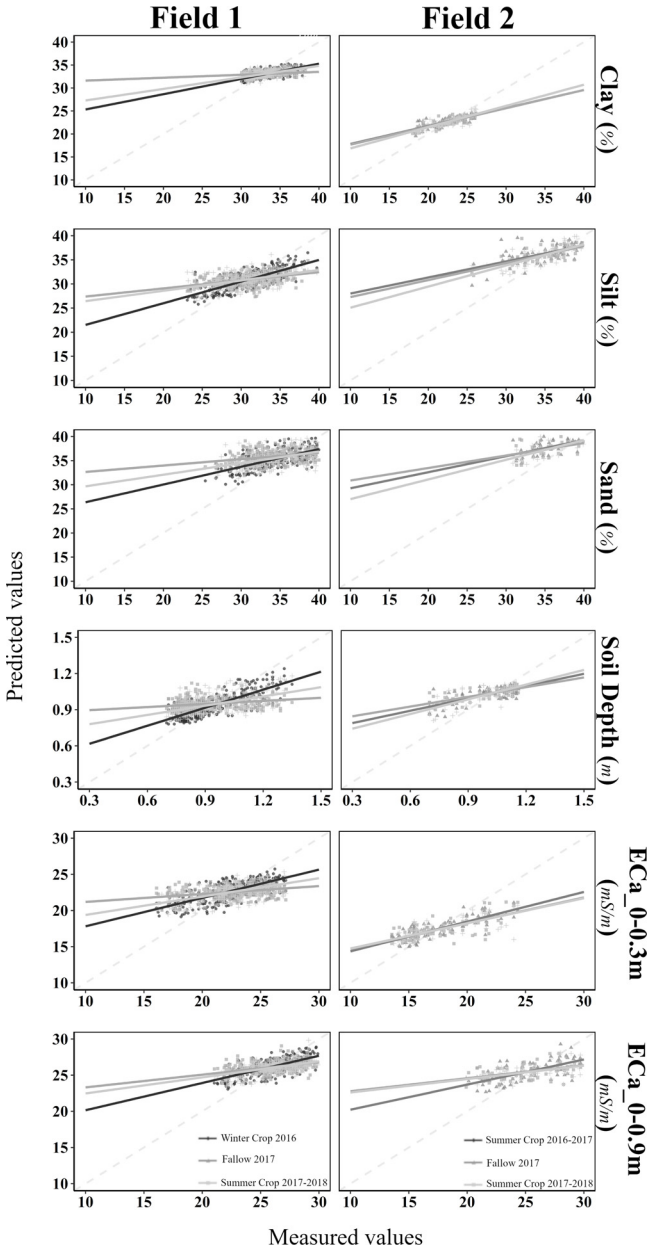

Fig. 7. Scatter plots of the predicted and measured soil properties by field and coverage condition.

backscattering time series allow determining partly spatio-temporal dynamics of phenological events until the soybean flowering stage; (*ii*) that NDVI temporal series allow analyzing and interpreting the dynamics of SAR backscatter temporal series; and (*iii*) the effect of soybean maturity on the SAR backscattering. After R2 phenological development stage, soybean starts drying out, leaves fall and decrease the leaf area index. So, when the fresh biomass decreases, a lower attenuation of the SAR backscattering is generated, and consequently it is mostly affected by soil conditions. According to that, Baup et al. (2015) reported that VH and VV polarizations were less sensitive during soybean senescence stage because their values did not decrease when crop moisture content decreased. Also, McNairn et al. (2014) reported that VH and VV polarizations of phenological periods previous full seed (phenological stages < R2) result more precise to identify soybean crop in the coverage classification at a regional scale.

Table 2
Root Mean Square Error (RMSE) and Lins´s Concordance Correlation Coefficient (ρc) for all soil properties prediction by field and coverage condition.

Field	Soil property	*RMSE*	ρ_c	*RMSE*	ρ_c	*RMSE*	ρ_c
		Winter Crop 2016		**Fallow 2017**		**Summer Crop 2017 – 2018**	
Field 1	Clay content	1.41	0.53	1.81	0.11	1.53	0.43
	Silt content	2.46	0.64	3.20	0.31	3.12	0.36
	Sand content	3.07	0.66	4.31	0.21	3.83	0.42
	Soil depth	0.10	0.72	0.16	0.15	0.14	0.42
	ECa_0 – 0.3 m	1.87	0.59	2.46	0.19	2.15	0.42
	ECa_0 – 0.9 m	1.56	0.61	1.96	0.32	1.84	0.4
		Summer Crop 2016 – 2017		**Fallow 2017**		**Summer Crop 2017 – 2018**	
Field 2	Clay content	1.43	0.61	1.41	0.63	1.31	0.69
	Silt content	3.37	0.59	2.96	0.69	2.89	0.71
	Sand content	4.40	0.61	4.10	0.67	4.00	0.68
	Soil depth	0.10	0.55	0.11	0.46	0.10	0.63
	ECa_0 – 0.3 m	1.88	0.64	2.10	0.56	2.07	0.56
	ECa_0 – 0.9 m	2.70	0.5	2.96	0.36	2.83	0.42

3.3. Predictive performance of the RF algorithm

Table 1 shows the percentage of explained variance for each soil property from RF regressions executed by field and coverage condition (crop or fallow).

In field 1, the explained variance for each soil property was between 47.2 and 69.12 % for the winter crop 2016, between 10.45 and 27.78 % for the summer crop 2017 – 2018 and between 34.09 and 40.54 % for the fallow 2017. The highest explained variance was that for effective soil depth, followed by that for silt content during the winter crop 2016, while the lowest one was that for clay content during the fallow 2017. In the field 2, the explained variance was between 41.49 and 57.70 % for the summer crop 2017 – 2018, between 30.02 and 61.87 % for the fallow 2017, and between 36.11 and 65.67 % for the summer crop 2016 – 2017. The prediction accuracy of SAR backscattering during the fallow 2017 was noticeably different between fields. This can be explained by the dynamics of production and decomposition of the harvest residue biomass (Zheng et al., 2014). In field 1, the crop previous to fallow was wheat, whereas, in field 2, the crop during the last four months before fallow was sunflower. Thus, the difference in the backscattering is due to a different of production of residue biomass between fields. Several studies have reported that radar backscattering of multiple SAR bands might be sensitive to changes in the composition of crop residues during the fallow season. McNairn et al. (2002), for example, reported dominant backscattering mechanisms in the C-band, associated with the type and amount of crop residues. Also, McNairn et al. (2001) analyzed the sensitivity of the C-band and L-band radar backscattering to variations in the amount of residues of corn and barley. These authors reported that the magnitude of the effect of residues on SAR backscattering depends on the residue moisture, decomposition and volume and determined that cross-polarized backscattering is more sensitive to the residue dynamics of winter and summer crops (Zheng et al., 2014).

3.3.1. Importance of radar SAR backscattering and DPSVI

Figs. 5 and 6 show the SAR backscattering and DPSVI with high prediction accuracy of soil properties in fields 1 and 2, respectively, obtained from the RF regression model. For field 1, the VH polarization on September 30th and November 29th 2016, and the VV polarization on November 5th and November 29th 2016, had the highest prediction accuracy of soil properties (Fig. 5). Particularly, the VV polarizations on November 5th and November 29th 2016 were the images with highest prediction accuracy for effective soil depth, silt content and sand content. For field 2, the VV polarization on October 24th and November

29th 2016 during Summer Crop 2016 – 2017 period and the VV polarization on November 24th 2016 and on February 28th 2017 during Summer Crop 2017 – 2018, showed the highest prediction accuracy had the highest prediction accuracy of soil properties (Fig. 6). Particularly, the VV polarizations on November 24th, December 6th 2017 and February 28th 2018, were the images with highest prediction accuracy for effective soil depth, silt content and clay content.

In general, VV and VH in this order were those SAR data with high prediction accuracy of soil properties in both and coverage conditions. Specifically, the VV and VH polarizations with high prediction accuracy attained radar backscattering values lower than -10 and -20 dB, respectively. In field 1, the polarizations mentioned showed the highest predictive accuracy of soil properties during the development stage of wheat particularly in three conditions. First, at the tillering stage (30/Sep/2016) when LAI is less than 3 and the number of stems per m^2 is less than 500 (Satorre and Slafer, 1999). In that context, plants have low height and poor attenuation. Thus, VH and VV polarizations are mainly affected by soil properties variations, which depend on soil moisture dynamics and surface roughness (Veloso et al., 2017). Second, at heading stage (5/Nov/2016) when LAI is more than 4 and the number of stems per m^2 is less than 700. The volume fraction of the vegetation is maximum at hearing as a result of the maximum growth in the number of stems per plant and in the length of these stems. In addition, at this stage occurs the highest hydric demand of the crop. In that situation, VV polarization which have the highest predictive accuracy of soil properties are mainly influenced by the vertical structures of wheat stems (Brown et al., 2003). Changes in spatio-temporal dynamics of these structures become a potential aspect to predict soil properties through VV polarizations. Third, at the ripening stage and senescence (29/Nov/2016) during which the increase on SAR backscatter is as a consequence of the decreasing chlorophyll and water content.

In field 2, C-Band SAR data showed a high predictive accuracy of soil properties during the development stage for both summer crop periods in three conditions. First, after germination stage in the 2016 – 2017 period (Soybean crop, 24/Oct/2016). This may be explained by the fact that the height of soybean is low, only a few leaves are fully developed and the number of stems is low, which leads to a poor attenuation of backscattering signal. Thus, at this moment the backscatter responses mainly depends on the soil moisture content and surface roughness. Second, at the highest growth-rate of soybean crop for both periods (29/Nov/2016 to summer crop 2016 – 2017 period and 24/Nov/2017 to summer crop 2017 – 2018 period, respectively). At this crop stage, in both periods the water availability was optimum with low SAR backscatter (VH < -20 and VV > -15, respectively). Under wet conditions, the interaction between crop and soil properties dominates the decrease of SAR backscatters in comparison to crop volume contribution (Baup et al., 2015; McNairn et al., 2014). Third, at the full seed and beginning maturity in the summer crop 2017 – 2018 period (28/Feb/2018). As was explained before, in low water availability conditions and at the beginning of the soybean senescence the interaction between crop and soil properties leads to higher SAR backscatter. Thus, the water storage determined the biomass dynamic and thus, the SAR backscattering behavior (Veloso et al., 2017).

So, the results of this section are relevant because (*i*) it was demonstrated that the process of variable selection using RF regression allow to indentify those SAR backscatters with high predictive accuracy of soil properties at field scale during the growing period of wheat, sunflower and soybean (Veloso et al., 2017); (*ii*) they show the effect of the interaction between biomass dynamics of wheat, sunflower and soybean crops, and soil water dynamics, on the accuracy of SAR backscattering to predict soil properties at field scale; and (*iii*) they allow defining the time of observation when the prediction accuracy of SAR backscattering is potentially applicable to several soil properties.

3.4. Prediction accuracy

Fig. 7 and Table 2 show a comparison between scatter plots of the predicted and measured soil properties, and a comparison of RMSE and ρ_c in the predictions of soil properties, by field and condition coverage, respectively. In field 1, the best predictions for all soil properties were achieved with SAR backscattering of wheat crop for the winter crop 2016 period (R^2 between 0.48 – 0.65; ρ_c between 0.53 – 0.72). Those predictions were less precise during the fallow 2017 (R^2 between 0.07 – 0.23; ρ_c between 0.11 – 0.32). Specifically, soil depth, sand and silt content, in that order were the properties better predicted ($R^2 > 0.58$). In field 2, the predictions more precise for all soil properties were achieved with SAR backscattering of both summer crop periods, being slightly more precise for the summer crop 2017 – 2018 period (R^2 between 0.47 – 0.66 Summer crop 2016 – 2017 period; R^2 between 0.44 – 0.74 Summer crop 2017 – 2018 period). Particularly, ECa_0 – 0.3 m, sand and clay content were the properties better predicted ($R^2 > 0.59$). In both fields, ρ_c were less than 0.72, indicating that predictions had a moderate and poor agreement.

Combining SAR backscattering temporal series, feature selection using RF and RF prediction can be considered as an efficient technique to predict ECa, texture and soil depth. Using this method was able to achieve RMSEs less than 1.81 and 4.4 %, for clay and sand content, respectively. Our RMSE values are lower than those have been reported in previous studies. Zribi et al. (2011) used an inversion model methodology based on X-Band SAR backscattering to predict clay content with an RMSE ~12.5 % for the prediction of that variable. Gorrab et al. (2015) used TerraSAR-X data to predict soil moisture and texture applying empirical linear models. They reported an RMSE ~10.8 and 18.6 % for clay and sand content, respectively. Clearly, the availability of C-band SAR data and the prediction scheme provides significant information to improve soil cartography at field scale.

4. Conclusions

In the present study, we presented, validated and tested a prediction scheme for topsoil properties at farm field scale by the combination of free and massive C-band SAR data, optical data, feature selection using RF and RF regression model. The prediction scheme involved: (*i*) the analysis of spatial-temporal dynamics of SAR backscattering, DPSVI and NDVI at field conditions in the southeast of Buenos Aires province, Argentina, during the crop and fallow periods; (*ii*) the evaluation of the predictive importance (feature selection) of SAR backscattering for the RF regression of multiple topsoil properties; (*iii*) the analysis of the relationship between the SAR backscattering and NDVI, according to their prediction accuracy for topsoil properties; and (*iv*), the analysis of the prediction accuracy.

In general, VH/VV ratio y DPSVI were useful representing the dynamics of biomass, but the efficiency was variable according to the crop type and soil moisture content. VH/VV ratio mainly represented the growing dynamics for wheat and soybean but not for sunflower. Also, spatio-temporal relationship among fresh biomass, NDVI and VH/VV ratio was dependent on the crop type and the interaction to soil moisture variation. In that context, DPSVI represented moderately sunflower and soybean dynamics but not was helpful for wheat crop. At present, relationship of spatio-temporal dynamics between DPSVI and wheat, sunflower and soybean developments have been poorly documented (Periasamy, 2018). SAR backscattering with high predictive accuracy of topsoil properties were efficiently selected using Feature selection with RF, reducing not only data with a poor predictive capacity or redundant but also computation time. The selection of SAR backscattering allow identifying key moments during the wheat and soybean developments in which SAR data had higher prediction accuracy of topsoil properties. Also, we can determined that in sunflower cropping conditions the SAR data prediction accuracy was notoriously decreasing. Predictions for clay, silt and sand soil content performed

based on the present prediction scheme result more efficient than those previously reported. Soil depth and sand content were the soil properties with high percentage of explained variance (> 65 % and > 40 %, respectively), for both fields and in all coverage conditions. In addition, we achieved efficient predictions for ECa and soil depth which is an unprecedented result. The Root Mean Square Error (RMSE) calculated for ECa and soil depth revealed the values between 0.1 − 0.16 m, and 1.56–2.96 mS m^{-1}, respectively. In mostly soil properties an overestimation of low values was detected.

The availability of C-band SAR data and prediction scheme use provides an opportunity to optimize methods of soil functional cartography for site-specific crop management applications. Further studies should propose, validate and evaluate viable and economic sampling schemes that are able to generate spatial predictions of soil properties with high performance. New radar vegetation indices should be validated as auxiliary information to predict soil properties. Additional studies are needed to test the relevance of the directional scattering and validate this approach in numerous farm-fields

CRediT authorship contribution statement

Marisa B. Domenech: Conceptualization, Methodology, Writing - original draft. **Nilda M. Amiotti:** Writing - review & editing. **José L. Costa:** Writing - review & editing. **Mauricio Castro-Franco:** Methodology, Software, Visualization, Writing - original draft.

Declaration of Competing Interest

The authors confirm and sign that there is no conflict of interests with networks, organizations and data centers referred in the paper.

References

Allen, R.G., Pereira, L.S., Raes, D., Smith, M., 1998. Crop Evapotranspiration-Guidelines for Computing Crop Water Requirements-FAO Irrigation and Drainage Paper 56. FAO, Rome 300, D05109.

Alvarez, R., 2009. Predicting average regional yield and production of wheat in the Argentine Pampas by an artificial neural network approach. Eur. J. Agron. 30, 70–77.

Alvarez, R., Lavado, R.S., 1998. Climate, organic matter and clay content relationships in the Pampa and Chaco soils, Argentina. Geoderma 83, 127–141.

Barral, M.P., Oscar, M.N., 2012. Land-use planning based on ecosystem service assessment: a case study in the Southeast Pampas of Argentina. Agric. Ecosyst. Environ. 154, 34–43.

Baup, F., Fieuzal, R., Betbeder, J., 2015. Estimation of soybean yield from assimilated optical and radar data into a simplified agrometeorological model. In: 2015 IEEE International Geoscience and Remote Sensing Symposium (IGARSS). IEEE. pp. 3961–3964.

Berger, M., Moreno, J., Johannessen, J.A., Levelt, P.F., Hanssen, R.F., 2012. ESA's sentinel missions in support of Earth system science. Remote Sens. Environ. 120, 84–90.

Birrell, S.J., Sudduth, K.A., Borgelt, S.C., 1996. Comparison of sensors and techniques for crop yield mapping. Comput. Electron. Agric. 14, 215–233. https://doi.org/10.1016/0168-1699(95)00049-6.

Boettinger, J.L., 2010. Digital Soil Mapping: Bridging Research, Production, and Environmental Application. Springer Science & Business Media.

Boettinger, J., Ramsey, R., Bodily, J., Cole, N., Kienast-Brown, S., Nield, S., Saunders, A., Stum, A., 2008. Landsat spectral data for digital soil mapping. Digital Soil Mapping with Limited Data. Springer, pp. 193–202.

Breiman, L., 2001. Random forests. Mach. Learn. 45, 5–32. https://doi.org/10.1023/a:1010933404324.

Brown, S.C., Quegan, S., Morrison, K., Bennett, J.C., Cookmartin, G., 2003. High-resolution measurements of scattering in wheat canopies-Implications for crop parameter retrieval. IEEE Trans. Geosci. Remote Sens. 41, 1602–1610.

Castro Franco, M., Costa, J.L., Peralta, N., Aparicio, V., 2015. Prediction of soil properties at farm scale using a model-based soil sampling scheme and random forest. Soil Sci. 180, 1–12.

Castro-Franco, M., Domenech, M.B., Borda, M.R., Costa, J.L., 2017. A spatial dataset of topsoil texture for the southern Argentine Pampas. Geoderma Reg. https://doi.org/10.1016/j.geodrs.2017.11.003.

Corwin, D.L., Lesch, S.M., 2003. Application of soil electrical conductivity to precision agriculture: theory, principles, and guidelines. Agron. J. 95, 455–471.

Corwin, D.L., Lesch, S.M., 2005. Characterizing soil spatial variability with apparent soil electrical conductivity: I. Survey protocols. Comput. Electron. Agric. 46, 103–133. https://doi.org/10.1016/j.compag.2004.11.002.

d'Andrimont, R., Taymans, M., Lemoine, G., Ceglar, A., Yordanov, M., van der Velde, M., 2020. Detecting flowering phenology in oil seed rape parcels with Sentinel-1 and -2 time series. Remote Sens. Environ. 239, 111660. https://doi.org/10.1016/j.rse.2020.111660.

Dang, Y., Pringle, M., Schmidt, M., Dalal, R., Apan, A., 2011. Identifying the spatial variability of soil constraints using multi-year remote sensing. Field Crops Res. 123, 248–258.

Della Maggiora, A.I., Irigoyen, A.I., Gardiol, J.M., Caviglia, O., Echarte, L., 2002. Evaluación de un modelo de balance de agua en el suelo para el cultivo de maíz. Evaluation of soil water balance model for maize. Rev. Argent. Agrometeorol. 2, 167–176.

Diggle, P.J., Ribeiro, P.J., 2007. Model Based Geostatistics. Springer Series in Stadistics, New York.

Domenech, M.B., Castro-Franco, M., Costa, J.L., Amiotti, N.M., 2017. Sampling scheme optimization to map soil depth to petrocalcic horizon at field scale. Geoderma 290, 75–82. https://doi.org/10.1016/j.geoderma.2016.12.012.

Gee, G., Bauder, J., 1986. Particle-size analysis. Methods of Soil Analysis. Part 1. Physical and Mineralogical Methods. pp. 383–411 Madison, WI.

Genuer, R., Poggi, J.-M., Tuleau-Malot, C., 2010. Variable selection using random forests. Pattern Recognit. Lett. 31, 2225–2236.

Gorelick, N., Hancher, M., Dixon, M., Ilyushchenko, S., Thau, D., Moore, R., 2017. Google earth engine: planetary-scale geospatial analysis for everyone. Remote Sens. Environ. 202, 18–27. https://doi.org/10.1016/j.rse.2017.06.031.

Gorrab, A., Zribi, M., Baghdadi, N., Mougenot, B., Fanise, P., Chabaane, Z.L., 2015. Retrieval of both soil moisture and texture using TerraSAR-X images. Remote Sens. 7, 10098–10116.

Grömping, U., 2009. Variable importance assessment in regression: linear regression versus random forest. Am. Stat. 63.

Han, D., Vahedifard, F., Aanstoos, J.V., 2017. Investigating the correlation between radar backscatter and in situ soil property measurements. Int. J. Appl. Earth Obs. Geoinf. 57, 136–144.

Hartemink, A.E., McBratney, A.B., de Lourdes Mendonça-Santos, M., 2008. Digital Soil Mapping with Limited Data. Springer Science + Business Media B.V.

INTA, 2010. Carta de Suelos de la Provincia de Buenos Aires. Instituto Nacional de Tecnología Agropecuaria, Buenos Aires - Argentina.

Kriegler, F.J., Malila, W.A., Nalepka, R.F., Richardson, W., 1969. Preprocessing transformations and their effects on multispectral recognition. Remote Sensing of Environment, VI. pp. 97.

Lagacherie, P., McBratney, A., Voltz, M., 2006. Digital Soil Mapping: An Introductory Perspective. Elsevier Science.

Liaw, A., Wiener, M., 2002. Classification and Regression by randomForest. R News 2. pp. 18–22.

Ließ, M., Glaser, B., Huwe, B., 2012. Uncertainty in the spatial prediction of soil texture: comparison of regression tree and Random Forest models. Geoderma 170, 70–79.

Lobell, D.B., Thau, D., Seifert, C., Engle, E., Little, B., 2015. A scalable satellite-based crop yield mapper. Remote Sens. Environ. 164, 324–333. https://doi.org/10.1016/j.rse.2015.04.021.

Mattia, F., Le Toan, T., Picard, G., Posa, F.I., D'Alessio, A., Notarnicola, C., Gatti, A.M., Rinaldi, M., Satalino, G., Pasquariello, G., 2003. Multitemporal C-band radar measurements on wheat fields. IEEE Trans. Geosci. Remote Sens. 41, 1551–1560.

McNairn, H., Shang, J., 2016. A review of multitemporal synthetic aperture radar (SAR) for crop monitoring. Multitemporal Remote Sensing. Springer, pp. 317–340.

McNairn, H., Duguay, C., Boisvert, J., Huffman, E., Brisco, B., 2001. Defining the sensitivity of multi-frequency and multi-polarized radar backscatter to post-harvest crop residue. Can. J. Remote Sens. 27, 247–263.

McNairn, H., Duguay, C., Brisco, B., Pultz, T.J., 2002. The effect of soil and crop residue characteristics on polarimetric radar response. Remote Sens. Environ. 80, 308–320. https://doi.org/10.1016/S0034-4257(01)00312-1.

McNairn, H., Kross, A., Lapen, D., Caves, R., Shang, J., 2014. Early season monitoring of corn and soybeans with TerraSAR-X and RADARSAT-2. Int. J. Appl. Earth Obs. Geoinf. 28, 252–259.

Minasny, B., McBratney, A.B., 2006. A conditioned Latin hypercube method for sampling in the presence of ancillary information. Comput. Geosci. 32, 1378–1388.

Pascale, A.J., Damario, E.A., 2004. Bioclimatología agrícola y agroclimatología. Editorial Facultad de Agronomía. Universidad de Buenos Aires, Buenos Aires, Argentina.

Pérez, S., Sierra, E., Momo, F., Massobrio, M., 2015. Changes in average annual precipitation in Argentina's pampa region and their possible causes. Climate 3, 150–167.

Periasamy, S., 2018. Significance of dual polarimetric synthetic aperture radar in biomass retrieval: an attempt on Sentinel-1. Remote Sens. Environ. 217, 537–549.

Periasamy, S., Senthil, D., Shanmugam, R.S., 2019. A Modified Triangle with SAR Target Parameters for Soil Texture Categorization Mapping, in: Advances in Remote Sensing and Geo Informatics Applications. Springer International Publishing, Cham, pp. 97–99.

R Core Team, 2016. R: a Language and Enviroment for Stadistical Computing. R Fundation for Stadistical Computing, Viena, Austria.

Robinson, G.W., 1922. A new method for the mechanical analysis of soils and other dispersions. J. Agric. Sci. 12, 306–321.

Roudier, P., Beaudette, D., Hewitt, A., 2012. A conditioned latin hypercube sampling algorithm incorporating operational constraints. In: Malone, Brendan P., McBratney, A.B. (Eds.), Digital Soil Assessments and Beyond, pp. 227–231.

Sadras, V.O., Calviño, P.A., 2001. Quantification of grain yield response to soil depth in soybean, maize, sunflower, and wheat. Agron. J. 93, 577–583. https://doi.org/10.2134/agronj2001.933577x.

Satorre, E.H., Slafer, G.A., 1999. Wheat production systems of the Pampas. Wheat Ecol. Physiol. Yield Determ. 333–348.

Song, Y., Wang, J., 2019. Mapping winter wheat planting area and monitoring its phenology using Sentinel-1 backscatter time series. Remote Sens. 11, 449.

Travasso, M.I., Suero, E.E., 1994. Estimación de la capacidad de almacenaje de agua en

suelos del sudeste bonaerense. Bol. Téc. 125, 9.
Van Ittersum, M.K., Cassman, K.G., Grassini, P., Wolf, J., Tittonell, P., Hochman, Z., 2013. Yield gap analysis with local to global relevance—A review. Field Crops Res. 143, 4–17.
Veloso, A., Mermoz, S., Bouvet, A., Le Toan, T., Planells, M., Dejoux, J.-F., Ceschia, E., 2017. Understanding the temporal behavior of crops using Sentinel-1 and Sentinel-2-like data for agricultural applications. Remote Sens. Environ. 199, 415–426. https://doi.org/10.1016/j.rse.2017.07.015.
Viscarra Rossel, R.A., Chen, C., Grundy, M.J., Searle, R., Clifford, D., Campbell, P.H., 2015. The Australian three-dimensional soil grid: Australia's contribution to the GlobalSoilMap project. Soil Res. 53, 845–864. https://doi.org/10.1071/SR14366.
Vreugdenhil, M., Wagner, W., Bauer-Marschallinger, B., Pfeil, I., Teubner, I., Rüdiger, C., Strauss, P., 2018. Sensitivity of Sentinel-1 backscatter to vegetation dynamics: an Austrian case study. Remote Sens. 10, 1396.
Zheng, B., Campbell, J.B., Serbin, G., Galbraith, J.M., 2014. Remote sensing of crop residue and tillage practices: present capabilities and future prospects. Soil Tillage Res. 138, 26–34. https://doi.org/10.1016/j.still.2013.12.009.
Zribi, M., Kotti, F., Lili-Chabaane, Z., Baghdadi, N., Issa, N.B., Amri, R., Amri, B., Chehbouni, A., 2011. Soil texture estimation over a semiarid area using TerraSAR-X radar data. IEEE Geosci. Remote Sens. Lett. 9, 353–357.